

**Supporting Information for**

**Transformation of the coordination complex  
[Co(C<sub>3</sub>S<sub>5</sub>)<sub>2</sub>]<sup>2-</sup> from a molecular magnet to a  
potential qubit**

Majed S. Fataftah, Scott C. Coste, Bess Vlasisavljevich, Joseph M. Zadrozny,  
Danna E. Freedman\*

<sup>†</sup>*Department of Chemistry, Northwestern University, Evanston, Illinois 60208-  
3113*

*The Royal Society of Chemistry, Chemical Science*

## Table of Contents:

<b>Experimental Details</b>	<b>S4</b>
<b>Table S1:</b> Crystallographic information of <b>1</b>	<b>S13</b>
<b>Table S2:</b> Crystallographic information of <b>3</b>	<b>S14</b>
<b>Table S3:</b> Crystallographic information of <b>4</b>	<b>S15</b>
<b>Table S4:</b> Tabulated magnetic parameters for <b>1 – 4</b> from fitting magnetic susceptibility	<b>S16</b>
<b>Table S5:</b> Tabulated magnetic parameters for <b>1 – 4</b> from fitting Magnetization curves	<b>S16</b>
<b>Table S6:</b> Tabulated magnetic parameters for <b>1 – 4</b> from computational studies	<b>S16</b>
<b>Table S7:</b> SO-CASPT2 calculated first 8 states of the zero-field splitting	<b>S17</b>
<b>Table S8:</b> Tabulated Cole-Cole fit parameters for <b>1</b>	<b>S18</b>
<b>Table S9:</b> Tabulated Cole-Cole fit parameters for <b>2'</b>	<b>S19</b>
<b>Table S10:</b> Tabulated Cole-Cole fit parameters for <b>3</b>	<b>S20</b>
<b>Table S11:</b> Tabulated Cole-Cole fit parameters for <b>4</b>	<b>S21</b>
<b>Table S12:</b> Tabulated fit parameters for temperature dependent magnetic relaxation	<b>S22</b>
<b>Figure S1:</b> 100 K variable-field magnetization of <b>1, 3, and 4.</b>	<b>S23</b>
<b>Figure S2:</b> Variable-temperature dc magnetic susceptibility data for <b>1, 3, and 4</b> with fits.	<b>S24</b>
<b>Figure S3:</b> Variable-temperature, variable-field magnetization data for <b>1, 3, and 4.</b>	<b>S25</b>
<b>Figure S4:</b> Ac data for <b>1</b> under zero applied magnetic field	<b>S26</b>
<b>Figure S7:</b> Ac data for <b>d<sub>20</sub>-2</b> under zero applied magnetic field	<b>S27</b>
<b>Figure S5:</b> Ac data for <b>3</b> under zero applied magnetic field	<b>S28</b>
<b>Figure S6:</b> Ac data for <b>4</b> under zero applied magnetic field	<b>S29</b>
<b>Figure S8:</b> Arrhenius fit to <b>1</b>	<b>S30</b>
<b>Figure S9:</b> Arrhenius fit to <b>2</b>	<b>S31</b>
<b>Figure S10:</b> Arrhenius fit to <b>d<sub>20</sub>-2</b>	<b>S32</b>
<b>Figure S11:</b> Arrhenius fit to <b>3</b>	<b>S33</b>
<b>Figure S12:</b> Arrhenius fit to $\tau_s$ for <b>4</b>	<b>S34</b>
<b>Figure S13:</b> Arrhenius fit to $\tau_f$ for <b>4</b>	<b>S35</b>
<b>Figure S14:</b> Overlay of QTM frequency versus Co $\cdots$ Co and Co $\cdots$ H distances	<b>S36</b>

<b>Figure S15:</b> Overlay of $\nu_{\text{QTM}}$ and $D$ versus dihedral angle	<b>S37</b>
<b>Figure S16:</b> Zeeman plots simulated at L-band frequency along x-, y-, and z-directions	<b>S38</b>
<b>Figure S17:</b> L-band background cw EPR spectrum	<b>S39</b>
<b>Reference</b>	<b>S40</b>

## Experimental Details.

**General Considerations.** All compounds were manipulated and handled under a dinitrogen atmosphere in a Vacuum Atmospheres Nexus II glovebox. All glassware was either oven-dried at 150 °C for at least 4 hours or flame-dried prior to use. Acetonitrile (MeCN), tetrahydrofuran (THF), and diethylether (Et<sub>2</sub>O) were dried using a commercial solvent purification system from Pure Process Technology and stored over 3 or 4 Å sieves for a minimum of one day prior to use. Methanol (MeOH) was dried using the commercial solvent purification system followed by distillation under dinitrogen prior to use. Deuterated MeCN was purchased from Cambridge Isotope Labs, deoxygenated by three successive freeze-pump-thaw cycles, filtered through a pad of activated alumina, and stored over 4 Å sieves prior to use. CoCl<sub>2</sub> was prepared from CoCl<sub>2</sub>•6H<sub>2</sub>O by following the method of Horvath as applied for preparation of MnCl<sub>2</sub>.<sup>1</sup> 4,5-bis(benzoylthio)1,3-dithiole-2-thione (benzoyl dmit) was prepared according to literature procedures.<sup>2</sup> (Ph<sub>4</sub>P)<sub>2</sub>[Co(C<sub>3</sub>S<sub>5</sub>)<sub>3</sub>] (**1**) and the deuterated counterion, d<sub>20</sub>-Ph<sub>4</sub>P were synthesized according to previously reported procedures.<sup>3,4,5</sup> d<sub>20</sub>-Ph<sub>4</sub>P•**2** was synthesized in an identical manner to its protiated analogue, using d<sub>20</sub>-Ph<sub>4</sub>P<sup>+</sup> as the counterion. All other chemicals were used as received.

**(Bu<sub>4</sub>N)<sub>2</sub>[Co(C<sub>3</sub>S<sub>5</sub>)<sub>3</sub>] (**1**).** NaOMe (215 mg, 3.98 mmol) was combined with benzoyl dmit (862 mg, 2.12 mmol) in 10 mL of MeOH and was allowed to stir for an hour to yield a dark red solution, to which CoCl<sub>2</sub> (128 mg, 0.99 mmol) was added and allowed to stir for two hours. A solution of Bu<sub>4</sub>NBr (660 mg, 2.05 mmol) in 2 mL of MeOH was added dropwise leading to the formation of a dark purple precipitate. The mixture was stored in the freezer at -35C overnight leading to the formation of purple block shaped crystals. The crystals were filtered and washed with 10 mL of Et<sub>2</sub>O. The crystals were redissolved in approximately 15 mL hot MeCN, filtered

through diatomaceous earth, after which Et<sub>2</sub>O was slowly diffused into the solution to produce dark purple block shaped crystals (336 mg, 36.8 %) suitable for X-ray diffraction. IR (cm<sup>-1</sup>): 3054(w), 3037(w), 3016(w), 2985(w), 1582(s), 1482(s), 1434(vs), 1405(vs), 1338(m), 1311(m), 1185(m), 1160(m), 1104(vs), 1051(s), 1025(vs), 994(vs), 894(m), 848(w), 838(w), 752(s), 717(vs), 682(vs), 643(w) 615(w), and 519(vs). Anal. Calcd. for C<sub>40</sub>H<sub>75</sub>N<sub>3</sub>S<sub>10</sub>Co: 47.17 %C; 7.40 %H; 2.89 %N. Found: 47.49 %C; 7.03 %H; 3.00 %N.

**(PPN)<sub>2</sub>[Co(C<sub>3</sub>S<sub>5</sub>)<sub>2</sub>] (3).** NaOMe (54.4 mg, 1.00 mmol) was combined with benzoyl dmit (200.8 mg, 0.49 mmol) in 15 mL of MeOH and was allowed to stir for an hour yielding a dark red solution, at which time CoCl<sub>2</sub> (31.4 mg, 0.24 mmol) in 5 mL of MeOH was added and allowed to stir over night. Neat PPNCl (281.4 mg, 0.49 mmol) was added to the reaction mixture leading to the formation of a microcrystalline solid. The mixture was stirred for an additional hour, then filtered at which point the resulting magenta solid was washed with 30 mL of MeOH then 10 mL of Et<sub>2</sub>O. The collected solid was dried and weighed to be 326.0 mg of crude product. The crude product was then redissolved in MeCN and filtered through diatomaceous earth. Et<sub>2</sub>O was then allowed to diffuse into the MeCN solution to produce dark magenta elongated plates shaped crystals. IR (cm<sup>-1</sup>): 3050(w), 1587(w), 1481(m), 1435(m), 1405(m), 1299(m), 1279(m), 1260(s), 1180(w), 1162(w), 1112(s), 1053(m), 1027(s), 997(m), 928(w), 897(w), 850(w), 800(w), 742(m), 720(vs), 690(vs), 615(w), 531(vs), 506(s), 496(vs), 463(m), and 446(w). Anal. Calcd. for C<sub>78</sub>H<sub>60</sub>CoN<sub>2</sub>P<sub>4</sub>S<sub>10</sub>: 61.28 %C; 3.96 %H; 1.83 %N. Found: 60.98 %C; 3.89 %H; 1.82 %N.

**[(18c6)K]<sub>2</sub>[Co(C<sub>3</sub>S<sub>5</sub>)<sub>2</sub>] (4)** KOMe (101.8 mg, 1.45 mmol) and benzoyl dmit (297.1 mg, 0.73 mmol) were stirred in 15 mL of MeOH for an hour yielding a dark red solution. CoCl<sub>2</sub> (47.5mg, 0.37 mmol) in 2 mL of MeOH was subsequently added to the reaction mixture and allowed to stir for an hour at which point 18-crown-6 (208.5 mg, 0.79 mmol) in 2 mL of MeOH was added

to the solution. The resulting solution was allowed to stir overnight. After removal of the solvent *in vacuo*, 20 mL of THF was added to the solid residue. The mixture was then stirred briefly, then pumped down to dryness *in vacuo* followed by further drying at 65°C for 2 h. This procedure was repeated twice. The solid was then redissolved in THF and filtered through diatomaceous earth. Et<sub>2</sub>O was allowed to diffuse into the resulting THF solution to produce dark magenta elongated plate-like crystals. IR (cm<sup>-1</sup>): 2885(m), 2864(m), 2821(w), 2743(w), 1468(w), 1451(w), 1415(m), 1349(sh), 1282(w), 1247(w), 1099(vs), 1049(s), 1025(vs), 999(m), 958(m), 891(m), 834(m), 771(w), 522(w), 461(sh). Anal. Calcd. for C<sub>38</sub>H<sub>64</sub>CoO<sub>14</sub>S<sub>10</sub>K<sub>2</sub>: 37.95 %C; 5.36 %H. Found: 38.12 %C; 5.30 %H.

**Magnetic Measurements.** Magnetic data were collected using a Quantum Design MPMS-XL SQUID magnetometer. Measurements for all compounds were obtained on finely ground microcrystalline powders. The compounds were restrained in a frozen eicosane matrix and flame sealed in a quartz tube under vacuum or wrapped tightly within a polyethylene bag. In this latter case, the sample was prepared under a dinitrogen atmosphere and transferred to the SQUID in a Schlenk tube under a flow of Ar gas. Dc susceptibility measurements were collected in the temperature range 1.8–300 K under dc fields of 0.1, 0.5 and 1 T. Dc magnetization measurements were performed under applied magnetic fields of 1, 2, 3, 4, 5, 6 and 7 T in the temperature range of 1.8–10 K. Dc magnetic susceptibility data were corrected for diamagnetic contributions from the sample holder and eicosane as well as for the core diamagnetism of each sample, estimated using Pascal's constants.<sup>6</sup> Ac susceptibility were performed on all compounds in the temperature range of 1.8 K to 15 K, between frequencies of 1 to 1500 Hz with an oscillating magnetic field of 4 Oe at zero-applied dc field. Prior to full characterization, variable dc field magnetization data was collected from 0 to 4 T at 100 K to ensure the absence of

curvature associated with ferromagnetic impurities. Errors reported in Figures S4 and S5 on the magnetic parameters for simulation of the dc magnetic data were attained via successive simulation of the data in search for the upper and lower limits on the values before the simulation deviated from the experimental data significantly, by maintain the residual sum of errors below the value of 0.1.

**X-ray Diffraction.** Single crystal diffraction data collections were performed on single crystals coated with Paratone-N oil and mounted on a MicroMounts<sup>TM</sup> rod. The crystals were frozen while coated in Paratone-N oil under a stream of N<sub>2</sub> during the measurement. Structures for **1**, **2**, **4**, **5** were collected with a Bruker KAPPA APEX-II diffractometer equipped with a Mo K $\alpha$  ( $\lambda = 0.71073$  Å) sealed tube diffraction source with a graphite monochromater, and a Bruker APEX-II detector. Data for **3** were collected on a MICROSTAR X-ray source of Cu K $\alpha$  ( $\lambda = 1.54056$  Å) radiation with a Bruker SMART APEX CCD area detector. Raw data were integrated and corrected for Lorentz and polarization effects using Bruker Apex2 v. 2013.<sup>7</sup> Absorption corrections were applied using SADABS.<sup>8</sup> Space group assignments were determined by examination of systematic absences, *E*-statistics, and successive refinement of the structures. The crystal structure was solved by direct methods with the aid of successive difference Fourier maps in SHELXS<sup>9</sup> operated with the OLEX2 interface.<sup>10</sup> The crystals showed no significant decay during data collection. Thermal parameters were refined anisotropically for all non-hydrogen atoms in the main body, solvents of crystallization, and counterions. Hydrogen atoms were placed in ideal positions and refined using a riding model for all structures.

**L-Band EPR spectroscopy Measurements.** L-band (1.367-1.388 GHz) EPR spectroscopy was performed in the National Biomedical EPR Facility at the Medical College of Wisconsin (MCW) on a home built instrument, the details of which are described elsewhere.<sup>11</sup> Samples were finely

ground powders restrained in eicosane and sealed under vacuum in Wilmad 4 mm outer diameter quartz tubes. The magnetic field was calibrated with the  $g = 2.0036$  resonance of 2,2-diphenyl-1-picrylhydrazyl (DPPH). Spectra were recorded with 10 dB microwave power attenuation (0.1 mW incident power at 1.36 GHz) and 0.4 mT (4 G) with field modulation at 100 kHz. Spectra of 30 s scan time with a time constant of 0.064 ms were averaged over a period of 3 minutes at 110 K and background spectra were recorded on samples of frozen 18 M $\Omega$  water (Millipore) to ensure confidence in sample signal assignment.

**All Other Physical Measurements.** Combustion analysis of all complexes was performed by Midwest Microlab (Indianapolis, IN). Infrared spectra were recorded on a Bruker Alpha FTIR spectrometer equipped with an attenuated total reflectance accessory. Solution-phase NMR spectra were collected with an Agilent Au 400 MHz spectrometer. Proton NMR spectra are referenced to CDCl<sub>3</sub> at 7.26 ppm. UV-vis spectra were collected on a Varian Cary 5000 spectrometer in MeCN.

**Computational Details.** Complete active space self-consistent field calculations with corrections from second order perturbation theory (CASSCF/CASPT2) were performed on the experimental geometry for complexes **1-4**.<sup>12-14</sup> The active space included the 3d and 4d orbitals on the cobalt center and the eight valence electrons resulting in an (8e,10o) active space. Scalar relativistic effects were treated through the use of the Douglas-Kroll-Hess (DKH) Hamiltonian<sup>15,16</sup> and ANO-RCC basis sets of triple- $\zeta$  quality were employed with the following contractions: 6s5p3d2f1g for cobalt and 5s4p2d1f for sulfur, and 4s3p2d1f for carbon<sup>17,18</sup> Higher CI roots were computed in order to include the lowest lying excited states which is essential if one wishes to obtain reliable magnetic properties. To this end, electronic states consisting of excitations in the full  $d$ -manifold were included for a total of 40 doublet and 10 quartet states. CASPT2

calculations were performed for each spin-free state as implemented in the Molcas 8.0 software package.<sup>19</sup> Cholesky decomposition was used in combination with local exchange (LK) screening to reduce the cost of the two electron integrals.<sup>20</sup> Spin orbit coupling effects were computed a posteriori using the state interaction approach (RAS-SI).<sup>21</sup> The diagonal elements of this effective Hamiltonian were replaced with the CASPT2 energies in the so-called SOCASPT2 approach. The RASSI spin-orbit states that were obtained were then introduced into the SINGLE-ANISO module in order to calculate the magnetic properties ( $g$ ,  $D$ , and  $E$ ) of the complexes.<sup>22</sup>

**Discussion of fitting temperature dependence of  $\tau$ .** The temperature dependence of  $\tau$  was fit for **1** – **4** under zero applied magnetic field accounting for only two contributors to relaxation. Quantum tunneling of magnetization serves as a temperature independent relaxation process that dominates the relaxation at the lowest temperature of measurement, as indicated by the plateau in the relaxation profiles. The curvature observed in the temperature dependence of  $\tau$  at higher temperatures can be adequately fit by the inclusion of a Raman process, imparting a  $T^n$  dependence on the relaxation behavior. However, careful consideration of the exponent is required. For all variable-temperature relaxation data collected under zero-applied magnetic field, the Raman exponent was held constant at  $n = 5$ , as expected for complexes in which a ground spin multiplets state is present owing to coupling between nuclear and electronic spins of the  $\text{Co}^{2+}$  center. Improvements to the fits can be attained by allowing the exponent to vary, whereby it fluctuates between 4.5 and 5.5 for the **1** – **4**. The only relaxation profile which necessitated the inclusion of an Orbach process is the fast relaxation process ( $\tau_f$ ) in **4**. However, it is worth noting the significant errors associated with  $\tau_f$  at higher temperatures owing to the difficulty in resolving the fast relaxation process above 20 K.

Fitting the slow component of the temperature relaxation profile of **4** ( $\tau_s$ ) can proceed by either inclusion of an Orbach relaxation mechanism, as presented in Figure 3c of the manuscript, by excluding, as presented in Figure S12. Both fits yield a similar goodness-of-fit parameter, with minor discrepancies, where the sum of the squared residuals (SSR) was 1.4 vs 1.36 for the fits with and without the Orbach process, respectively. Inclusion of the Orbach process was performed by fitting the maximum number of high temperature data points, while holding the Raman exponent constant at  $n = 5$ . Inclusion of data points below 22 K led to deviation of the Raman exponent from  $n = 5$ . The  $U_{\text{eff}}$  value reported in the manuscript therefore represents the lower limit by including the maximum number of data points.

**Discussion of exclusion of dipolar coupling from QTM.** Three factors facilitate and permit quantum tunneling of magnetization through the double well potential in single-molecule magnets: transverse anisotropy ( $E$ ), exchange interactions, and dipolar coupling to nearby nuclear and electronic spins. In compounds **1** – **4**, in order to correlate  $E$  with the QTM frequency, the deuterated analogue of **2**,  $(\text{d}^{20}\text{-Ph}_4\text{P})_2[\text{Co}(\text{C}_3\text{S}_5)_2]$ , was synthesized and investigated by ac susceptibility under zero-applied dc magnetic field. The variable-temperature relaxation profile was identical to its protiated analogue, **2**. Due to the lack of exchange interactions in these mononuclear complexes, dipolar interactions were the only consideration. Due to the absence of nuclear spins in the immediate ligand field, there are two nuclear spin contributors remaining, the nuclear spin of the cobalt itself, which cannot be controlled for, and those originating from counterions. Compound **2** possesses the closest  $\text{Co}\cdots\text{H}$  through-space distance of 2.998(2) Å relative to **1**, **3** and **4** possessing 3.208(3) Å and 3.035(3) Å and 3.098(1) Å distances, respectively. Furthermore, the shortest  $\text{Co}\cdots\text{Co}$  intermolecular distance of 8.66(1) Å in **2** was that present in **2** as well. This permitted us to exclude the convoluting influence of counterion nuclear

spins as well as intermolecular electronic dipolar interactions between adjacent cobalt spin centers from our analysis.

**Modelling L-band cw spectrum.** Owing to the well-isolated lowest lying Kramers doublet ( $M_S = \pm 3/2$ ), no contributions from  $M_S = \pm 1/2$  Kramers doublet are apparent in the cw spectrum, and the large energy separation between the two Kramers doublet ( $\Delta = 2D \sim 320 \text{ cm}^{-1}$ ) no inter-Kramers are possible at the frequency measurement. Due to these considerations, the cw EPR spectrum presented in Figure 5 in the main manuscript can be phenomenologically described using an effective spin model,  $S' = 1/2$ , with rhombic  $g$ -values hyperfine coupled to the  $I = 7/2$  cobalt nucleus ( $^{59}\text{Co}$ , 100 %  $I = 7/2$  abundant). The cw-EPR spectrum was modeled in EasySpin<sup>23</sup> using the effective spin Hamiltonian,  $\hat{H}' = \mu_B g'_i \mathbf{S}\mathbf{H} + \mathbf{I}\mathbf{A}'_i \mathbf{S}$  ( $i = x, y, z$ ), with the following parameters:  $g'_x = 0.79(5)$ ,  $g'_y = 0.84(3)$ ,  $g'_z = 6.8(2)$ ,  $A'_x = 142(1) \text{ MHz}$ ,  $A'_y = 149(1) \text{ MHz}$ ,  $A'_z = 2026(1) \text{ MHz}$ . The effective  $g$ -values and hyperfine ( $A'$ ) parameters can be transformed back to the  $S = 3/2$   $g$ -values and  $A$  constants using the rhombicity factor ( $\eta = E/D$ ) determined by computation,  $\eta = 0.015$ , using previous reported methods.<sup>24</sup> The new  $S = 3/2$  Hamiltonian parameters are:  $g_x = 2.37$ ,  $g_y = 2.52$ ,  $g_z = 2.26$ ,  $A_x = 426 \text{ MHz}$  ( $1.42 \times 10^{-2} \text{ cm}^{-1}$ ),  $A_y = 447 \text{ MHz}$  ( $1.49 \times 10^{-2} \text{ cm}^{-1}$ ).  $A_z = 675 \text{ MHz}$  ( $2.25 \times 10^{-2} \text{ cm}^{-1}$ ). Determination of rhombicity from the effective spin Hamiltonian parameters determined above is complicated by the  $g$ -value, which is heavily intertwined with the value of  $|E/D|$ . Therefore accurate determination of the rhombicity factor without accurate  $g$ -values for the  $S = 3/2$  model is difficult and unreliable.

Noteworthy, the spectrum cannot be accurately simulated in EasySpin as an  $S = 3/2$  complex with large, negative  $D$  and a small  $E$  because the simulations include transitions from the  $M_S = \pm 1/2$  Kramers doublet. Owing to the extremely weak intensities of the transitions observed at L-

band frequency, low Boltzmann population of the  $M_S = \pm 1/2$  Kramers doublet leads to signals that originate between the  $M_S = \pm 1/2$  states, and overwhelm the signals originating from the lowest energy Kramers doublet. These signals are most likely not observed experimentally due to the fast spin-lattice relaxation of the excited  $M_S$  Kramers doublet.<sup>25</sup> Because  $T_1$  relaxation times is not a parameter EasySpin accounts for in simulation of cw-EPR spectra, the spectrum is best modelled using an effective spin model, as described above.

**Table S1.** Crystallographic information for the structural refinement of **1**.

Empirical Formula	C <sub>38</sub> H <sub>72</sub> CoN <sub>2</sub> S <sub>10</sub>
Formula weight	1171.48 g/mol
Temperature	100(2) K
Wavelength	0.71073 Å
Crystal System	Monoclinic
Space Group	C2/c
Unit Cell Dimensions	$a = 18.3767(16)$ Å, $\alpha = 90.0^\circ$ $b = 8.6094(7)$ Å, $\beta = 100.972(5)^\circ$ $c = 31.158(3)$ Å, $\gamma = 90.0^\circ$
Volume	4839.5(8) Å <sup>3</sup>
Z	4
Density (calculated)	1.285 Mg/m <sup>3</sup>
Absorption coefficient	0.81 mm <sup>-1</sup>
$F_{000}$	1211.9
Crystal color	Red
Crystal size	0.21 × 0.19 × 0.15 mm <sup>3</sup>
$\theta$ range	2.76 to 52.48°
Index ranges	-11 ≤ $h$ ≤ 11 -20 ≤ $k$ ≤ 21 -23 ≤ $l$ ≤ 21
Reflections collected	26262
Independent reflections	25142 [ $R_{\text{int}} = 0.0726$ ]
Completeness to $\theta = 52.48^\circ$	94.9 %
Absorption correction	Multi-scan
Maximum and minimum transmission	0.655 and 0.745
Refinement method	Full-matrix least-squares on $F^2$
Data / restraints / parameters	10963 / 10 / 235
Goodness-of-fit on $F^{2a}$	1.128
Final $R$ indices [ $I > 2\sigma(I) = 10408$ data] <sup>b</sup>	$R_1 = 5.91$ %, $wR_2 = 10.93$ %
$R$ indices (all data, 0.80 Å)	$R_1 = 7.91$ %, $wR_2 = 15.55$ %
Largest diff. peak and hole	0.45 and -0.39 e.Å <sup>-3</sup>

<sup>a</sup> GooF =  $[\sum[w(F_o^2 - F_c^2)^2] / (n-p)]^{1/2}$  where n is the number of reflections and p is the total

number of parameters refined. <sup>b</sup> $R_1 = \sum||F_o| - |F_c|| / \sum|F_o|$ ;  $wR_2 = [\sum[w(F_o^2 - F_c^2)^2] / \sum[w(F_o^2)^2]]^{1/2}$

**Table S2.** Crystallographic information for the structural refinement of **3**.

Empirical Formula	$C_{78}H_{60}CoN_2P_4S_{10}$
Formula weight	1171.48 g/mol
Temperature	100(2) K
Wavelength	0.71073 Å
Crystal System	Triclinic
Space Group	$P\bar{1}$
Unit Cell Dimensions	$a = 9.6547(4)$ Å, $\alpha = 90.0^\circ$ $b = 20.7112(11)$ Å, $\beta = 90.966(3)^\circ$ $c = 35.6907(15)$ Å, $\gamma = 90.0^\circ$
Volume	7135.7(6) Å <sup>3</sup>
Z	8
Density (calculated)	1.423 Mg/m <sup>3</sup>
Absorption coefficient	0.798 mm <sup>-1</sup>
$F_{000}$	3156
Crystal color	Red
Crystal size	0.21 × 0.19 × 0.15 mm <sup>3</sup>
$\theta$ range	2.76 to 52.48°
Index ranges	$-9 \leq h \leq 10$ $-20 \leq k \leq 7$ $-36 \leq l \leq 36$
Reflections collected	26553
Independent reflections	10408 [ $R_{int} = 0.0492$ ]
Completeness to $\theta = 52.48^\circ$	94.9 %
Absorption correction	Multi-scan
Maximum and minimum transmission	0.655 and 0.745
Refinement method	Full-matrix least-squares on $F^2$
Data / restraints / parameters	10963 / 0 / 856
Goodness-of-fit on $F^{2a}$	1.062
Final $R$ indices [ $I > 2\sigma(I) = 10408$ data] <sup>b</sup>	$R_1 = 4.56$ %, $wR_2 = 10.68$ %
$R$ indices (all data, 0.80 Å)	$R_1 = 6.64$ %, $wR_2 = 12.28$ %
Largest diff. peak and hole	0.643 and $-0.632$ e.Å <sup>-3</sup>

<sup>a</sup> GooF =  $[\sum[w(F_o^2 - F_c^2)^2] / (n-p)]^{1/2}$  where n is the number of reflections and p is the total

number of parameters refined. <sup>b</sup> $R_1 = \sum||F_o| - |F_c|| / \sum|F_o|$ ;  $wR_2 = [\sum[w(F_o^2 - F_c^2)^2] / \sum[w(F_o^2)^2]]^{1/2}$

**Table S3.** Crystallographic information for the structural refinement of **4**.

Empirical Formula	$C_{56}H_{43}CoNP_2S_{10}$
Formula weight	1171.48 g/mol
Temperature	100(2) K
Wavelength	0.71073 Å
Crystal System	Monoclinic
Space Group	$P2_1/c$
Unit Cell Dimensions	$a = 9.8761(16)$ Å, $\alpha = 90.0^\circ$ $b = 17.519(3)$ Å, $\beta = 92.211(5)^\circ$ $c = 37.115(6)$ Å, $\gamma = 90.0^\circ$
Volume	6423.7(18) Å <sup>3</sup>
Z	8
Density (calculated)	1.392 Mg/m <sup>3</sup>
Absorption coefficient	0.78 mm <sup>-1</sup>
$F_{000}$	2832.0
Crystal color	Red
Crystal size	0.21 × 0.19 × 0.15 mm <sup>3</sup>
$\theta$ range	2.76 to 52.48°
Index ranges	$-12 \leq h \leq 11$ $-19 \leq k \leq 21$ $-45 \leq l \leq 45$
Reflections collected	40791
Independent reflections	8264 [ $R_{int} = 0.0492$ ]
Completeness to $\theta = 52.48^\circ$	99.8 %
Absorption correction	Multi-scan
Maximum and minimum transmission	0.192 and 0.259
Refinement method	Full-matrix least-squares on $F^2$
Data / restraints / parameters	12230 / 0 / 677
Goodness-of-fit on $F^{2a}$	1.098
Final $R$ indices [ $I > 2\sigma(I) = 10408$ data] <sup>b</sup>	$R_1 = 8.88$ %, $wR_2 = 30.64$ %
$R$ indices (all data, 0.80 Å)	$R_1 = 13.24$ %, $wR_2 = 26.47$ %
Largest diff. peak and hole	0.72 and $-0.73$ e.Å <sup>-3</sup>

<sup>a</sup> GooF =  $[\sum[w(F_o^2 - F_c^2)^2] / (n-p)]^{1/2}$  where n is the number of reflections and p is the total number of parameters refined. <sup>b</sup>  $R_1 = \sum||F_o| - |F_c|| / \sum|F_o|$ ;  $wR_2 = [\sum[w(F_o^2 - F_c^2)^2] / \sum[w(F_o^2)^2]]^{1/2}$

**Table S4.** Fit parameters to the variable-temperature magnetic susceptibility of **1 – 4**.

Compound	$ D $ (cm <sup>-1</sup> )	$E$ (cm <sup>-1</sup> )	$g_{\parallel}$	$g_{\perp}$
<b>1</b>	123(4)	0	3.04(5)	2.18(2)
<b>2</b>	127(3)	0	3.1(3)	2.34(5)
<b>3</b>	119(6)	0	3.02(6)	2.07(3)
<b>4</b>	130(4)	0	3.07(4)	2.11(6)

**Table S5.** Fit parameters to the variable-temperature, variable-field magnetization curves for **1 – 4**.

Compound	$D$ (cm <sup>-1</sup> )	$E$ (cm <sup>-1</sup> )	$g_{\text{iso}}$
<b>1</b>	-187(6)	0	3.06(4)
<b>2</b>	-161(8)	0	3.24(5)
<b>3</b>	-177(5)	0	2.95(5)
<b>4</b>	-166(10)	0	3.06(5)

**Table S6.** Zero-field splitting parameters ( $D$  &  $E$ ) and isotropic  $g$ -value for **1 – 4** computed at the SO-CASPT2 level of theory. The full manifold of 40 doublet states and 10 quartet states were included in the calculation. Values for  $D$  and  $E$  are reported in wavenumbers.

Compound	$D$ (cm <sup>-1</sup> )	$E$ (cm <sup>-1</sup> )	$g_{\text{iso}}$
<b>1</b>	-113.7	1.828	3.160
<b>2</b>	-116.4	1.147	3.219
<b>3</b>	-105.7	1.242	3.159
<b>4</b>	-118.0	0.988	3.275

**Table S7.** The first eight states of the zero-field splitting computed at the SO-CASPT2 level of theory including excitations in the full  $d$ -manifold. Energies are referenced to the lowest states in the series and are reported in  $\text{cm}^{-1}$ . The ninth state lies between 3900 and 4300  $\text{cm}^{-1}$  above the eighth state.

SO-State	<b>1</b>	<b>2</b>	<b>3</b>	<b>4</b>
1	490	185	0	1249
2	490	185	0	1249
3	717	418	212	1486
4	717	418	212	1486
5	1231	910	796	1959
6	1231	910	796	1959
7	1536	1220	1085	2275
8	1536	1220	1085	2275

**Table S8.** Cole-Cole plot fitting parameters for **1** under 0 Oe dc applied field.  $\chi_T$  and  $\chi_S$  are the isothermal and adiabatic magnetic susceptibilities, respectively.  $\chi_T$  therefore takes on the value of  $\chi'_M$  in the low-frequency limit, while  $\chi_S$  takes on the value of  $\chi'_M$  in the high-frequency limit.

Temperature (K)	$\chi_T$ (cm <sup>3</sup> /mol)	$\chi_S$ (cm <sup>3</sup> /mol)	$\tau$ (s)	$\alpha$
1.8	5.75	1.34	$1.55 \times 10^{-2}$	0.34
1.9	5.43	1.25	$1.42 \times 10^{-2}$	0.34
2	5.31	1.17	$1.51 \times 10^{-2}$	0.34
2.5	4.31	0.92	$1.39 \times 10^{-2}$	0.36
3.0	3.63	0.75	$1.40 \times 10^{-2}$	0.37
3.5	3.20	0.65	$1.42 \times 10^{-2}$	0.36
4.0	2.77	0.59	$1.25 \times 10^{-2}$	0.34
4.5	2.48	0.54	$1.04 \times 10^{-2}$	0.29
5.0	2.25	0.48	$8.22 \times 10^{-3}$	0.27
6.0	1.83	0.40	$4.10 \times 10^{-3}$	0.18
7.0	1.61	0.29	$2.09 \times 10^{-3}$	0.18
8.0	1.36	0.24	$1.04 \times 10^{-3}$	0.14
9.0	1.19	0.21	$5.81 \times 10^{-4}$	0.10
10.0	1.07	0.18	$3.54 \times 10^{-4}$	$8.7 \times 10^{-2}$

**Table S9.** Cole-Cole plot fitting parameters for **2'** (**d<sub>20-2</sub>**) under 0 Oe dc applied field.

Temperature (K)	$\chi_T$ (cm <sup>3</sup> /mol)	$\chi_S$ (cm <sup>3</sup> /mol)	$\tau$ (s)	$\alpha$
2	5.55	0.96	0.156	0.43
3	3.64	0.70	0.11	0.36
4	2.62	0.61	$4.61 \times 10^{-2}$	0.19
5	2.08	0.44	$1.59 \times 10^{-2}$	0.14
6	1.75	0.26	$6.25 \times 10^{-3}$	0.13
7	1.50	0.14	$2.78 \times 10^{-3}$	0.14
8	1.30	$6.98 \times 10^{-2}$	$1.42 \times 10^{-3}$	0.13
9	1.16	$6.76 \times 10^{-2}$	$8.58 \times 10^{-4}$	0.10
10	1.03	0	$5.44 \times 10^{-4}$	0.10
11	0.98	0	$3.71 \times 10^{-4}$	0
12	0.99	0	$2.61 \times 10^{-4}$	$8.28 \times 10^{-2}$
13	0.91	0	$1.89 \times 10^{-4}$	$6.1 \times 10^{-2}$
14	0.85	0	$1.41 \times 10^{-4}$	$5.5 \times 10^{-2}$
15	0.79	0	$1.07 \times 10^{-4}$	$3.6 \times 10^{-2}$

**Table S10.** Cole-Cole plot fitting parameters for **3** under 0 Oe dc applied field.

Temperature (K)	$\chi_T$ (cm <sup>3</sup> /mol)	$\chi_S$ (cm <sup>3</sup> /mol)	$\tau$ (s)	$\alpha$
1.8	5.93	0.99	0.12	0.38
1.9	5.55	1.11	0.13	0.34
2.0	4.81	0.90	0.12	0.35
2.5	4.08	0.79	0.12	0.34
3.0	2.83	0.65	$9.45 \times 10^{-2}$	0.26
3.5	2.46	0.47	$5.52 \times 10^{-2}$	0.23
4.0	2.14	0.41	$3.16 \times 10^{-2}$	0.19
4.5	1.89	0.39	$1.81 \times 10^{-2}$	0.13
5.0	1.67	0.44	$3.54 \times 10^{-3}$	$4.1 \times 10^{-2}$
6.0	1.14	$2.85 \times 10^{-2}$	$3.61 \times 10^{-3}$	0.23
7.0	0.93	$2.75 \times 10^{-2}$	$1.51 \times 10^{-3}$	0.19
8.0	0.81	0	$7.78 \times 10^{-4}$	0.16
9.0	0.72	0	$4.55 \times 10^{-4}$	0.14
10	0.64	0	$2.94 \times 10^{-4}$	0.12
11	0.62	$3.04 \times 10^{-2}$	$2.00 \times 10^{-4}$	0.11
12	0.54	0	$1.39 \times 10^{-4}$	$9.9 \times 10^{-2}$
13	0.50	0	$1.08 \times 10^{-4}$	$7.4 \times 10^{-2}$
14	0.45	0	$7.82 \times 10^{-5}$	0
15	0.43	0	$6.10 \times 10^{-5}$	0

**Table S11.** Cole-Cole plot fitting parameters for **4** under 0 Oe dc applied field.  $\chi_f$  and  $\chi_s$  are the isothermal susceptibilities for the fast and slow relaxation components, respectively, while  $\chi_0$  is the adiabatic susceptibility.

Temperature (K)	$\chi_s$ (cm <sup>3</sup> /mol)	$\alpha_s$	$\tau_s$ (s)	$\chi_f$ (cm <sup>3</sup> /mol)	$\alpha_f$	$\tau_f$ (s)	$\chi_0$ (cm <sup>3</sup> /mol)
1.8	9.0	0.22	2.37	11.4	0.65	2.76	0.15
1.9	9.3	0.28	2.72	12.6	0.65	3.91	0.16
2.0	9.1	0.27	2.70	12.4	0.65	4.17	0.15
2.5	6.9	0.29	2.43	9.8	0.63	2.46	0.12
3.0	5.0	0.35	1.94	7.9	0.60	1.14	0.12
3.5	4.8	0.39	1.42	7.4	0.57	0.72	0.11
4.0	3.2	0.38	0.82	5.0	0.55	0.27	0.10
4.5	2.8	0.88	0.40	2.4	0.50	6.0×10 <sup>-2</sup>	0.0
5.0	2.3	0.0	0.31	2.2	0.47	2.8×10 <sup>-2</sup>	0.10
6.0	1.88	0.0	0.13	1.6	0.43	1.0×10 <sup>-2</sup>	0.07
7.0	1.59	0.08	5.64×10 <sup>-2</sup>	1.1	0.36	3.2×10 <sup>-3</sup>	0.07
8.0	1.39	0.0	3.48×10 <sup>-2</sup>	1.0	0.40	2.0×10 <sup>-3</sup>	0.016
9.0	1.23	0.0	2.02×10 <sup>-2</sup>	0.80	0.37	1.1×10 <sup>-3</sup>	0.016
10	1.11	0.0	1.26×10 <sup>-2</sup>	0.73	0.36	6.1×10 <sup>-4</sup>	0.0
11	1.01	0.0	8.58×10 <sup>-3</sup>	0.64	0.34	3.9×10 <sup>-4</sup>	0.0
12	0.92	0.0	5.67×10 <sup>-3</sup>	0.56	0.30	2.5×10 <sup>-4</sup>	0.0
13	0.86	0.0	4.09×10 <sup>-3</sup>	0.51	0.28	1.9×10 <sup>-4</sup>	0.0
14	0.80	0.0	2.96×10 <sup>-3</sup>	0.48	0.29	1.4×10 <sup>-4</sup>	0.0
15	0.75	0.0	2.16×10 <sup>-3</sup>	0.45	0.32	1.1×10 <sup>-4</sup>	0.0
16	0.70	0.0	1.62×10 <sup>-3</sup>	0.40	0.26	7.1×10 <sup>-5</sup>	0.0
17	0.66	0.0	1.27×10 <sup>-3</sup>	0.39	0.26	5.9×10 <sup>-5</sup>	0.0
18	0.62	0.0	9.79×10 <sup>-4</sup>	0.37	0.27	5.5×10 <sup>-5</sup>	0.0
19	0.59	0.0	7.86×10 <sup>-4</sup>	0.33	0.29	3.9×10 <sup>-5</sup>	0.0
20	0.56	0.0	6.08×10 <sup>-4</sup>	0.31	0.30	3.5×10 <sup>-5</sup>	0.0
21	0.53	0.0	4.89×10 <sup>-4</sup>	0.28	0.18	2.7×10 <sup>-5</sup>	0.0
22	0.51	0.0	4.07×10 <sup>-4</sup>	0.27	0.19	2.3×10 <sup>-5</sup>	0.0
23	0.49	0.0	3.42×10 <sup>-4</sup>	0.26	0.19	1.8×10 <sup>-5</sup>	0.0
24	0.46	0.0	2.53×10 <sup>-4</sup>	0.23	0.19	1.1×10 <sup>-5</sup>	0.0
25	0.45	0.0	2.16×10 <sup>-4</sup>	0.21	0.19	5.0×10 <sup>-6</sup>	0.0
26	0.43	0.0	1.68×10 <sup>-4</sup>	0.18	0.19	1.0×10 <sup>-6</sup>	0.0

**Table S12.** Fitting parameters for the temperature dependent relaxation profile for **1 – 4**.

<b>Compound</b>	<b><i>A</i> (QTM)</b>	<b><i>B</i> (Raman)</b>	<b><i>n</i></b>	<b><i>C</i> (Orbach)</b>	<b><i>U</i><sub>eff</sub> (cm<sup>-1</sup>)</b>
<b>1</b>	61.75	2.63 x 10 <sup>-2</sup>	5	0	0
<b>2</b>	4.15	8.67 x 10 <sup>-3</sup>	5	0	0
<b>2'</b>	4.62	1.68 x 10 <sup>-2</sup>	5	0	0
<b>3</b>	6.5	2.94 x 10 <sup>-2</sup>	5	0	0
<b>4<sub>s</sub></b>	0.38	6.29 x 10 <sup>-4</sup>	5	0	0
<b>4<sub>s</sub> (alternate)</b>	0.26	4.5 x 10 <sup>-3</sup>	4.1	700000	130
<b>4<sub>f</sub></b>	0.12	3.17 x 10 <sup>-3</sup>	5.4	5 × 10 <sup>11</sup>	270

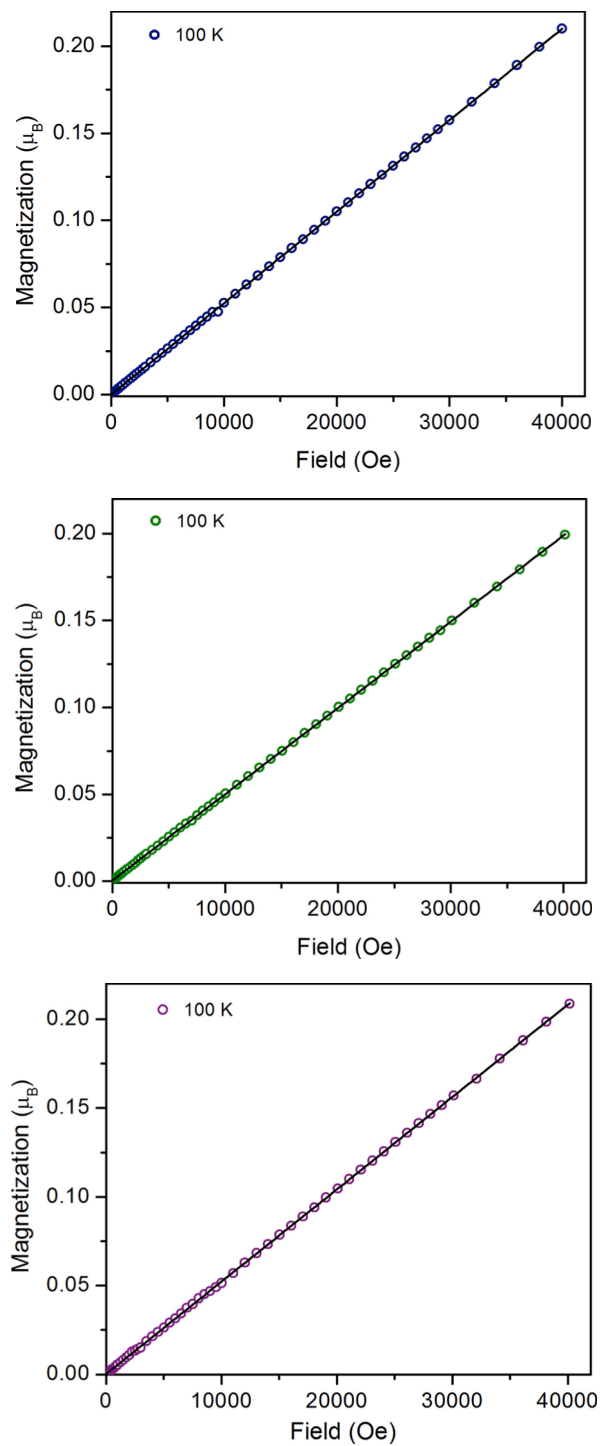


**Figure S1.** Variable-field magnetization of polycrystalline samples of **1**, **3** and **4** (top to bottom, respectively) restrained under eicosane acquired at 100 K. The black line is a linear fit to the data illustrating the absence of ferromagnetic impurities.

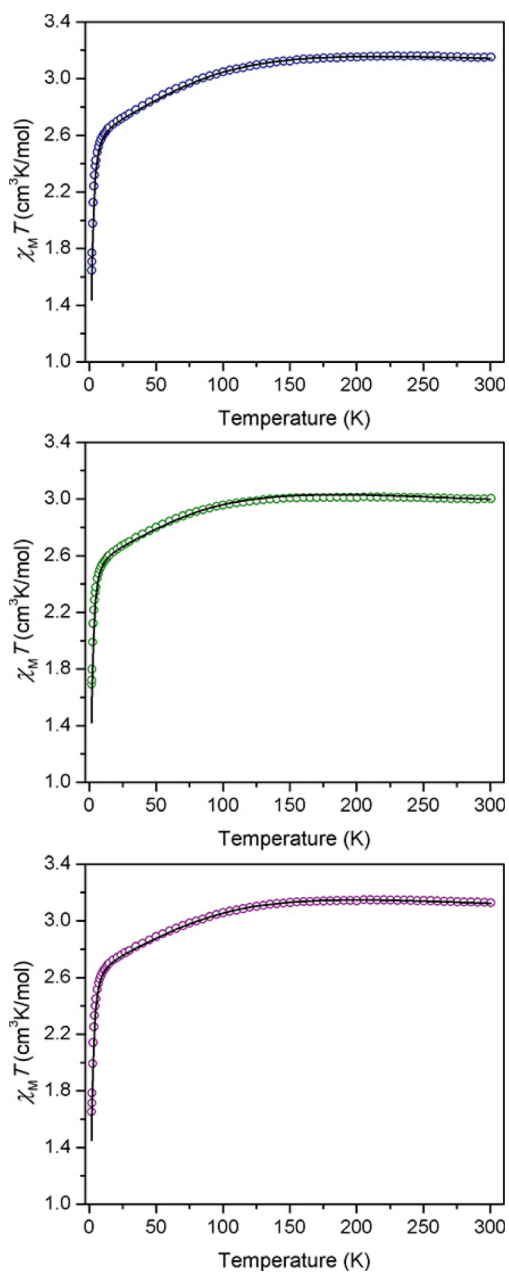


**Figure S2.** Variable-temperature dc magnetic susceptibility data for **1**, **3** and **4** (top to bottom respectively) collected from 1.8 K to 300 K under a dc field of 1 T. The black lines indicate simulated data obtained from the best fits to the 1 T data. The fits were performed using the spin Hamiltonian,  $\hat{H} = D\hat{S}_z^2 + E(\hat{S}_x^2 - \hat{S}_y^2) + (g_{\parallel} + g_{\perp})\mu_B\mathbf{S}\mathbf{H}$  in DAVE 2.0, with  $E$  constrained to a value of zero.

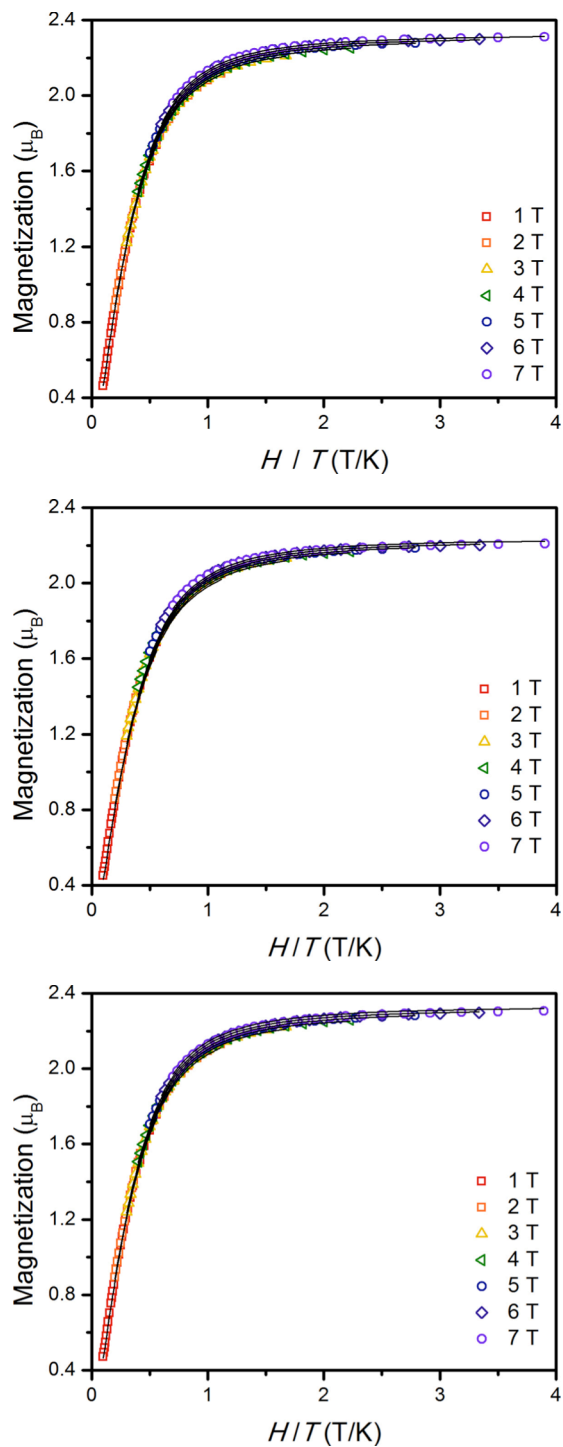


**Figure S3.** Variable-temperature, variable-field magnetization data for **1**, **3** and **4** (top to bottom, respectively) collected between 1.8 and 10 K from 1 to 7 T in 1 T increments. Black lines are simulations of the data obtained from fits using DAVE 2.0 and the spin Hamiltonian,  $\hat{H} = D\hat{S}_z^2 + E(\hat{S}_x^2 - \hat{S}_y^2) + g_{\text{iso}}\mu_B\mathbf{S}\mathbf{H}$ .  $E$  was held constant at zero throughout the fits owing to the low rhombicity ( $E/D \ll 0.1$ ).

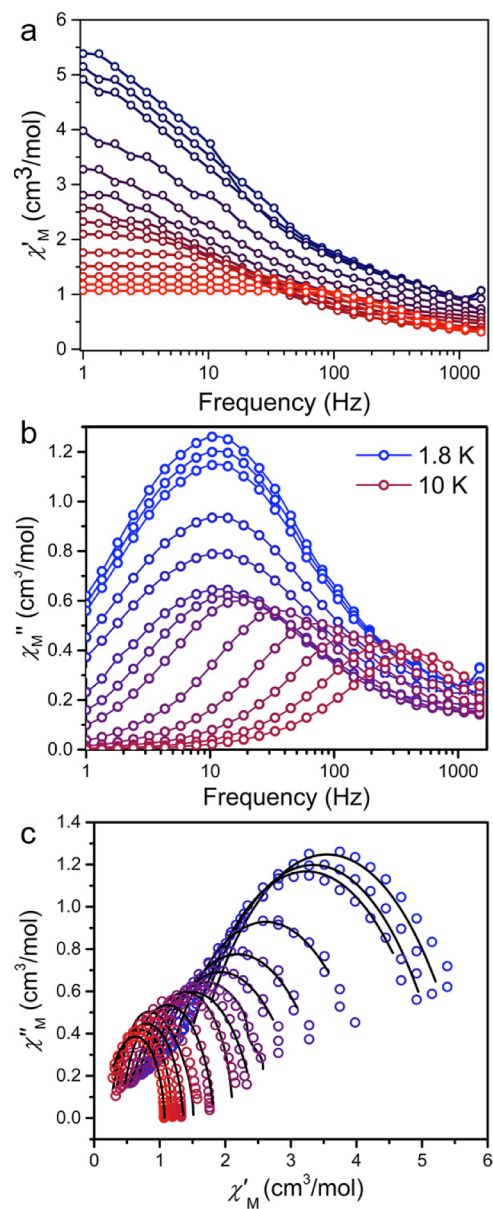


**Figure S4.** **a.** Variable-temperature, variable frequency in-phase ac susceptibility data collected under zero applied dc field in the temperature range of 1.8 to 10 K for **1**. The solid lines are guides for the eye. **b.** Variable-temperature, variable frequency out of phase ac susceptibility data collected under zero applied dc field in the temperature range of 1.8 to 10 K for **1**. The solid lines are guides for the eye. **c.** Cole-Cole plots for **1** under zero applied dc field. The plots were generated from the in-phase ( $\chi'_M$ ) and out of-phase ( $\chi''_M$ ) ac susceptibility data and fit using the generalized Debye model (black lines).

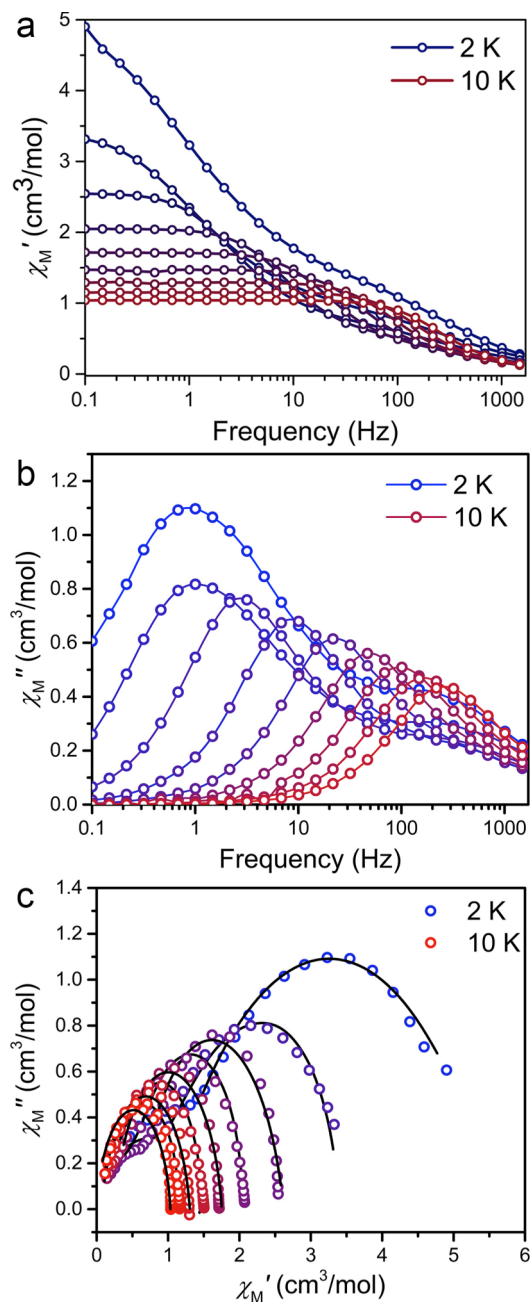


**Figure S5. a.** Variable-temperature, variable frequency in-phase ac susceptibility data collected under zero applied dc field in the temperature range of 1.8 to 26 K for  $2'$  ( $d_{20-2}$ ). The solid lines are guides for the eye. **b.** Variable-temperature, variable frequency out of phase ac susceptibility data collected under zero applied dc field in the temperature range of 1.8 to 26 K for  $d_{20-2}$ . The solid lines are guides for the eye. **c.** Cole-Cole plots for  $d_{20-2}$  under zero applied dc field. The plots were generated from the in-phase ( $\chi'_M$ ) and out of-phase ( $\chi''_M$ ) ac susceptibility data and fit using the generalized Debye model (black lines).

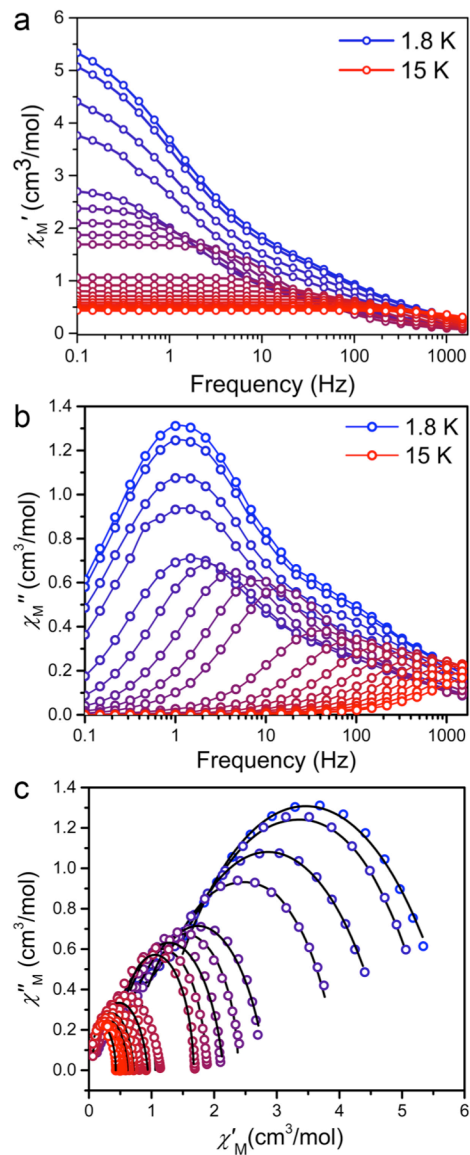


**Figure S6.** **a.** Variable-temperature, variable frequency in-phase ac susceptibility data collected under zero applied dc field in the temperature range of 1.8 to 15 K for **3**. The solid lines are guides for the eye. **b.** Variable-temperature, variable frequency out of phase ac susceptibility data collected under zero applied dc field in the temperature range of 1.8 to 15 K for **3**. The solid lines are guides for the eye. **c.** Cole-Cole plots for **3** under zero applied dc field. The plots were generated from the in-phase ( $\chi'_M$ ) and out of-phase ( $\chi''_M$ ) ac susceptibility data and fit using the generalized Debye model (black lines).

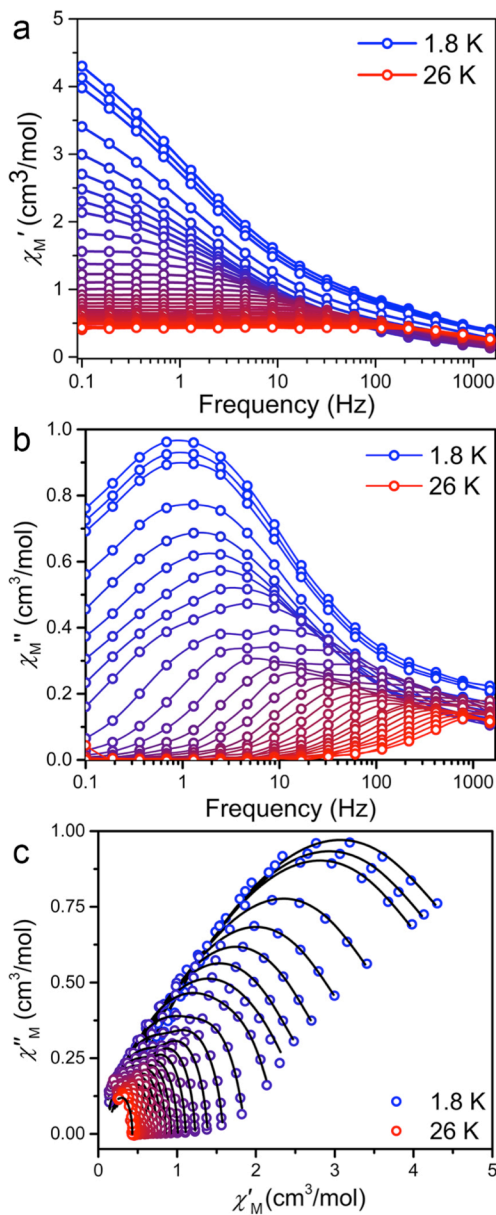


**Figure S7.** **a.** Variable-temperature, variable frequency in-phase ac susceptibility data collected under zero applied dc field in the temperature range of 1.8 to 26 K for **4**. The solid lines are guides for the eye. **b.** Variable-temperature, variable frequency out of phase ac susceptibility data collected under zero applied dc field in the temperature range of 1.8 to 26 K for **4**. The solid lines are guides for the eye. **c.** Cole-Cole plots for **4** under zero applied dc field. The plots were generated from the in-phase ( $\chi'_M$ ) and out of-phase ( $\chi''_M$ ) ac susceptibility data and fit using a two site generalized Debye model (black lines).

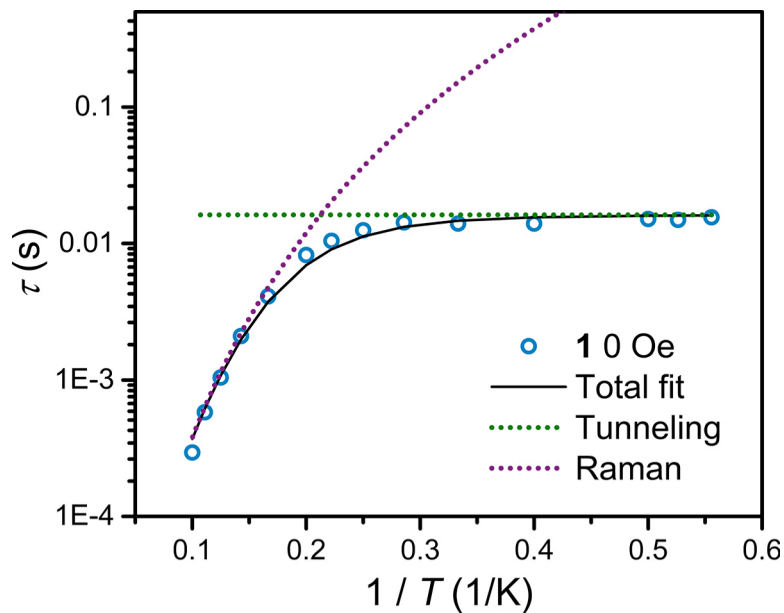


**Figure S8.** Fit to the variable temperature relaxation profile of **1** under zero applied dc field. The data were extracted from the Cole-Cole fits presented in Figure S4. The black line represents the total fit to the relaxation profile accounting for Raman (dotted purple line) and QTM (dotted green line) relaxation mechanisms.

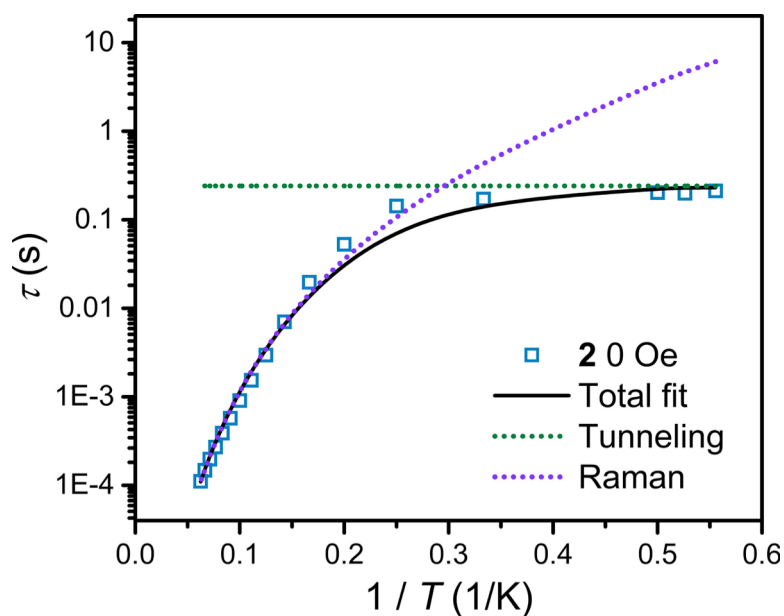


**Figure S9.** Fit to the variable temperature relaxation profile of **2** under zero applied dc field. The data were extracted from the Cole-Cole fits reported previously.<sup>3</sup> The black line represents the total fit to the relaxation profile accounting for Raman (dotted purple line) and QTM (dotted green line) relaxation mechanisms.

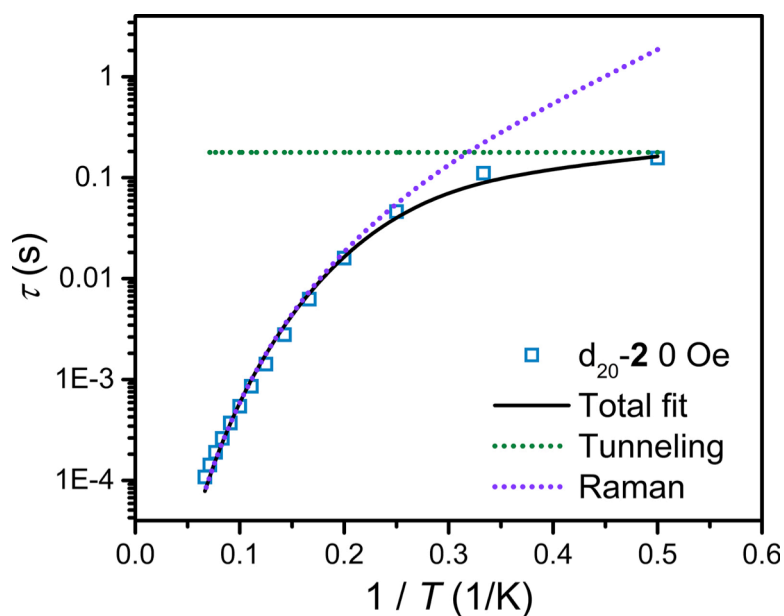


**Figure S10.** Fit to the variable temperature relaxation profile of  $d_{20-2}$  under zero applied dc field. The data were extracted from the Cole-Cole fits presented in Figure S7. The black line represents the total fit to the relaxation profile accounting for Raman (dotted purple line) and QTM (dotted green line) relaxation mechanisms.

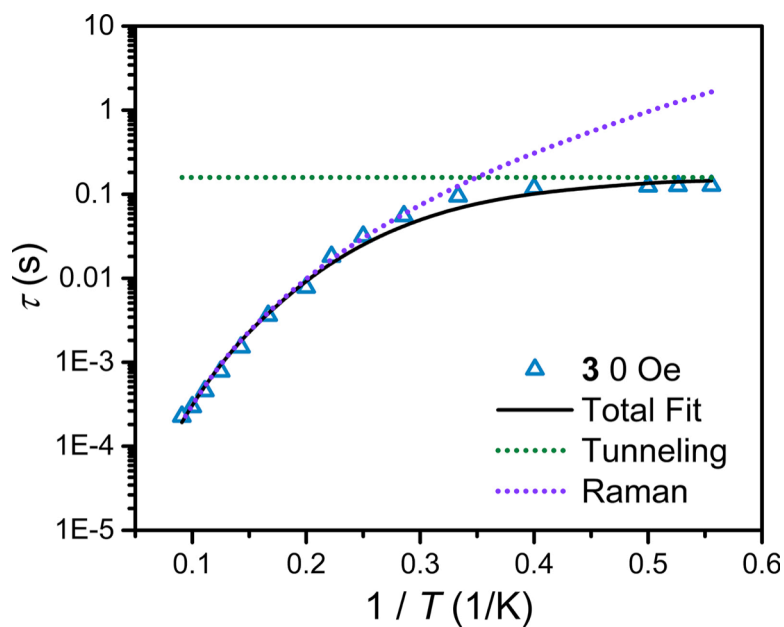


**Figure S11.** Fit to the variable temperature relaxation profile of **3** under zero applied dc field. The data were extracted from the Cole-Cole fits presented in Figure S5. The black line represents the total fit to the relaxation profile accounting for Raman (dotted purple line) and QTM (dotted green line) relaxation mechanisms.

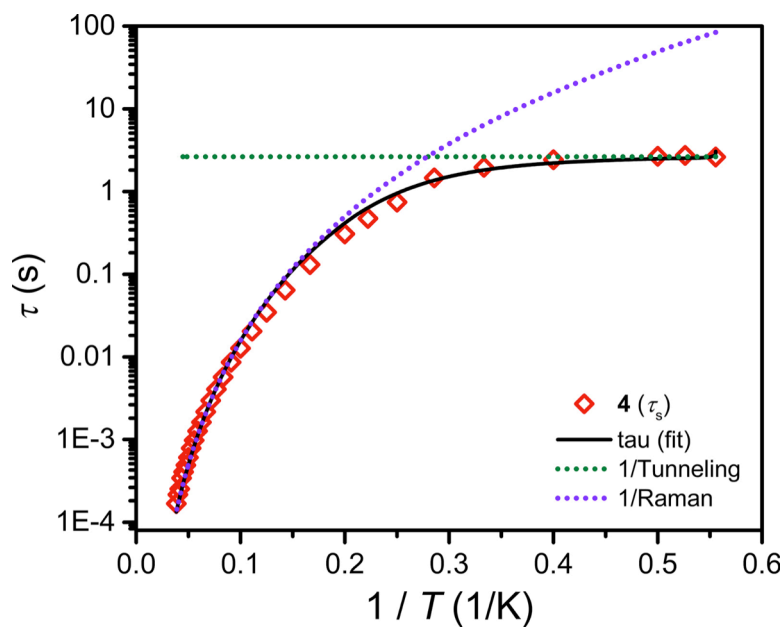


**Figure S12.** Fit to the variable temperature slow relaxation profile ( $\tau_s$ ) of **4** under zero applied dc field. This is an alternate fit to the data presented in the main manuscript in Figure 3c, excluding an Orbach process. The data were extracted from the Cole-Cole fits presented in Figure S6. The black line represents the total fit to the relaxation profile accounting for Raman (dotted purple line) and QTM (dotted green line) relaxation mechanisms.

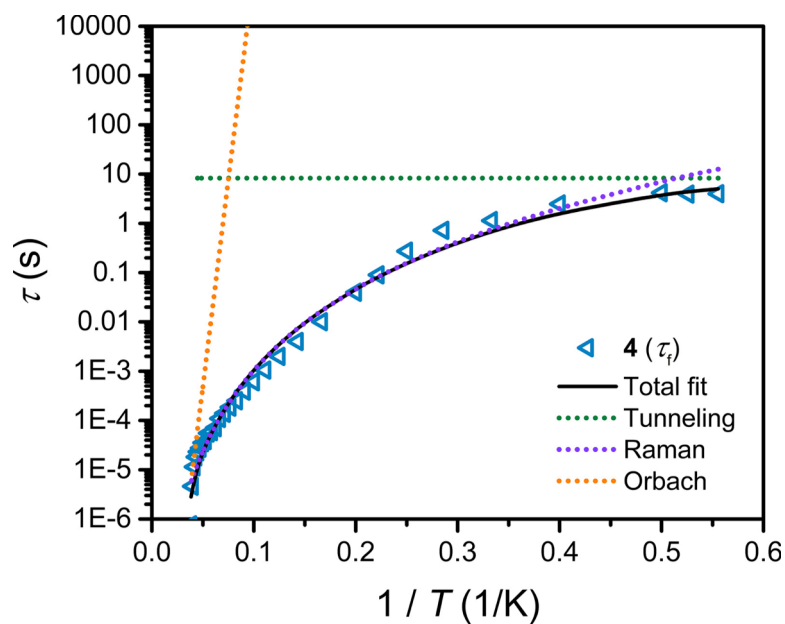


**Figure S13.** Fit to the variable temperature relaxation profile of the fast relaxation pathway for **4** under zero applied dc field. The data were extracted from the Cole-Cole fits presented in Figure S6. The black line represents the total fit to the relaxation profile accounting for Orbach (orange dotted line), Raman (dotted purple line) and QTM (dotted green line) relaxation mechanisms.

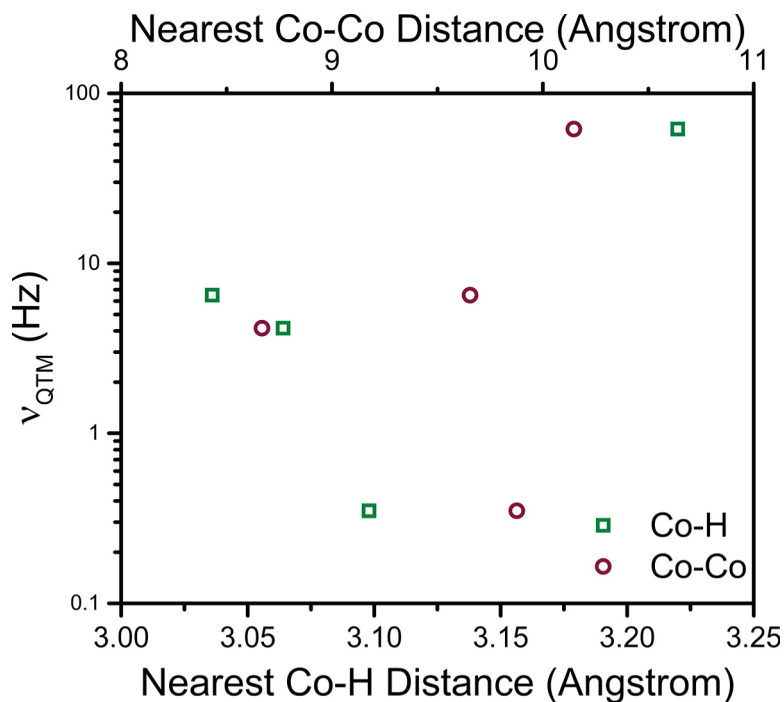


**Figure S14.** Overlay of nearest Co···Co and Co···H distances for **1** – **4** versus the quantum tunneling of magnetization frequency. The plot illustrates the absence of any trend across the series, whereby the complex with the fastest frequency possesses the longest Co···Co and Co···H distances.

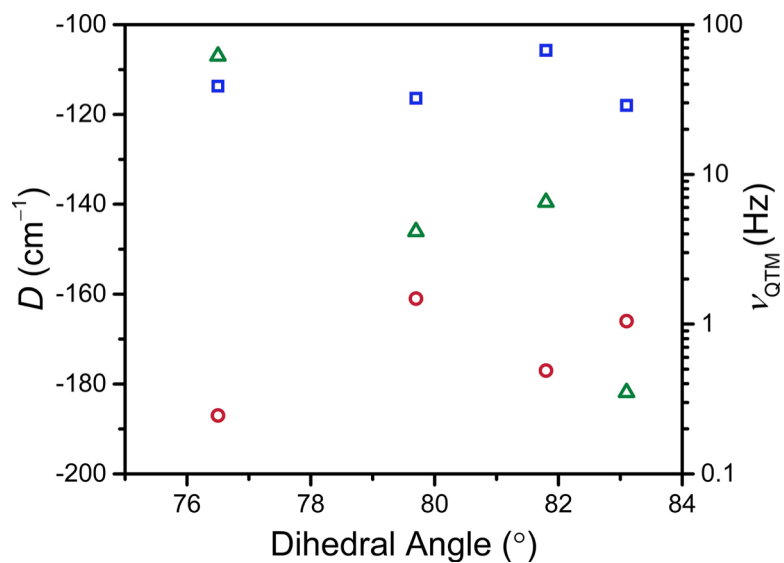


**Figure S15.** Overlay of the experimental (red circles) and calculated (blue squares) axial zero-field splitting ( $D$ , left axis) and  $\nu_{\text{QTM}}$  (green triangles, right axis) plotted as a function of the dihedral angle between the two planar  $\text{C}_3\text{S}_5^{2-}$  in  $[\text{Co}(\text{C}_3\text{S}_5)_2]^{2-}$  illustrating the absence of any trends.

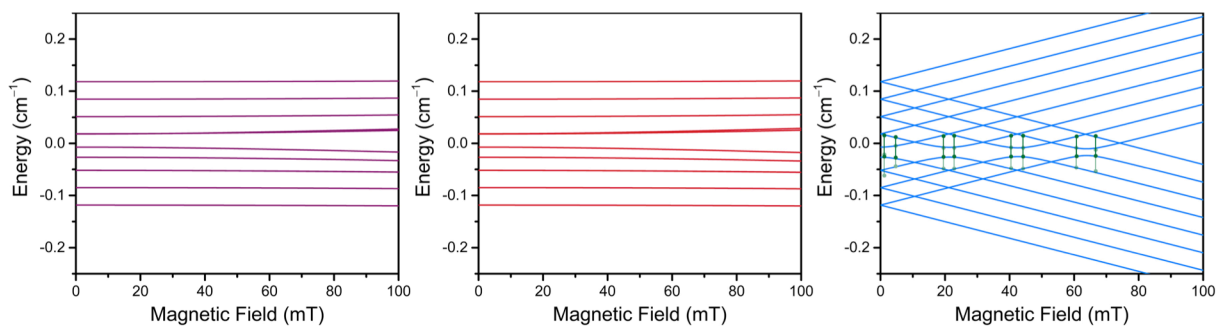


**Figure S16.** Left: Zeeman diagram simulated along the x-direction. Middle: Zeeman diagram simulated along the y-direction. Right: Zeeman diagram simulated along the z-direction. The green bars highlight the predicted transitions between the electro-nuclear hyperfine coupled states within the  $M_S = 3/2$  Kramers doublet. The Zeeman diagrams were simulated in EasySpin at L-band frequency ( $\nu = 1.368$  GHz) at 110 K. The diagrams were simulated using an effective spin Hamiltonian ( $S' = 1/2$ ) with the following effective  $g'$ -values and  $A'$  constants:  $g'_x = 0.79(5)$ ,  $g'_y = 0.84(3)$ ,  $g'_z = 6.8(2)$ ,  $A'_x = 142(1)$  MHz,  $A'_y = 149(1)$  MHz,  $A'_z = 2026(1)$  MHz.

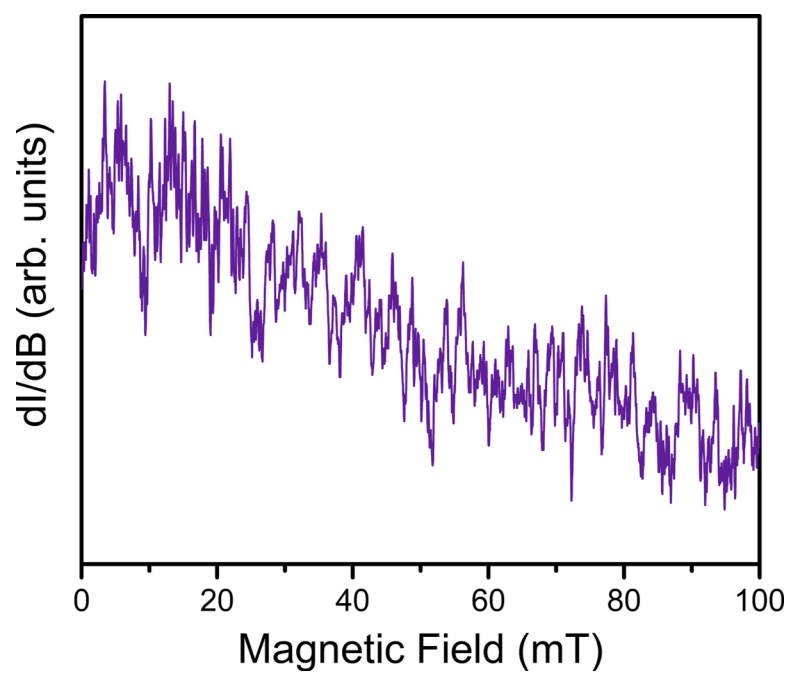


**Figure S17.** Cw-EPR spectrum of 18 M $\Omega$  water (Millipore) collected at L-band frequency ( $\nu = 1.368$  GHz) at 110 K. The spectrum was collected over the same number of scans and scan times as the experimental spectrum in Figure 5 to ensure confidence in signal assignment.

## References

1. B. Horvath, R. Mösel, and E. G. Horvath, *Z. Anorg. Allg. Chem.* 1979, **450**, 165.
2. T. K. Hansen, J. Becher, T. Jorgensen, K. S. Varma, R. Khedekar, and M. P. Cava, *Org. Synth.* 1996, **73**, 270.
3. M. S. Fataftah, J. M. Zadrozny, D. M. Rogers, D. E. Freedman, *Inorg. Chem.* 2014, **53**, 10716.
4. A. E. Carpenter, G. W. Margulieux, M. D. Millard, C. E. Moore, N. weidemann, A. L. Rheingold, and J. S. Figueroa, *Angew. Chem. Int. Ed.* 2012, **51**, 9412–9416.
5. D. Marcoux, and A. B. Charette, *J. Org. Chem.* 2008, **73**, 593.
6. G. A. Bain, and J. F. Berry, *J. Chem. Educ.* 2008, **85**, 532-536.
7. *APEX2*, v. 2009 ; Bruker Analytical X-Ray Systems, Inc: Madison, WI, 2009.
8. G. M. Sheldrick, *SADABS*, Version 2.03; Bruker Analytical X-ray Systems, Inc: Madison, WI, 2000.
9. G. M. Sheldrick, *SHELXTL*, Version 6.12; Bruker Analytical X-ray Systems, Inc: Madison, WI, 2000.
10. L. J. Farrugia, *J. Appl. Cryst.* 1999, **32**, 837-838.
11. J. S. Hyde, B. Bennett, E. D. Walter, G. L. Millhauser, G. W. Sidabras and W. E. Antholine, *Biophys. J.* 2009, **96**, 3354-3362.
12. B. O. Roos, P. R. Taylor, P. E. M. Siegbahn, *Chem. Phys.* 1980, **48**, 157.
13. K. Andersson, P. Malmqvist, B. Roos, A. J. Sadlej, K. Wolinski, *J. Phys. Chem.* 1990, **94**, 5483.
14. K. Andersson, P.-A. Malmqvist, B. O. Roos, *J. Chem. Phys.* 1992, **96**, 1218.
15. M. Douglas, N. M. Kroll, *Ann. Phys.* (N. Y). 1974, **82**, 89.
16. B. A. Hess, *Phys. Rev. A* 1986, **33**, 3742.
17. B. O. Roos, R. Lindh, P. Å. Malmqvist, V. Veryazov, P. O. Widmark, *J. Phys. Chem. A* 2004, **108**, 2851.
18. B. O. Roos, R. Lindh, P. Å. Malmqvist, V. Veryazov, P. O. Widmark, *J. Phys. Chem. A* 2005, **109**, 6575.
19. F. Aquilante,; L. De Vico, N. Ferre, G. Ghigo, P.-A. Malmqvist, P. Neogady, T. B. Pedersen, M. Pitonak, M. Reiher, B. O. Roos, L. Serrano-Andrés, M. Urban, V. Veryazov, R. Lindh, *J. Comput. Chem.* 2010, **31**, 224.
20. (a) Aquilante, F.; Pedersen, T. B.; Lindh, R. *J. Chem. Phys.* 2007, **126**, 194106. (b) Aquilante, F.; Lindh, R.; Pedersen, T. B. *J. Chem. Phys.* 2008, **129**, 034106. (c) Aquilante, F.; Malmqvist, P. Å.; Pedersen, T. B.; Ghosh, A.; Roos, B. O. *J. Chem. Theory Comput.* 2008, **4**, 694. (d) Aquilante, F.; Gagliardi, L.; Pedersen, T. B.; Lindh, R. *J. Chem. Phys.* 2009, **130**, 154107.
21. Malmqvist, P.-A.; Roos, B. O.; Schimmelpfennig, B. *Chem. Phys. Lett.* 2002, **357**, 230–240.
22. Aquilante, F.; De Vico, L.; Ferre, N.; Ghigo, G.; Malmqvist, P.- A.; Neogady, P.; Pedersen, T. B.; Pitonak, M.; Reiher, M.; Roos, B. O.; Serrano-Andres, L.; Urban, M.; Veryazov, V.; Lindh, R. *J. Comput. Chem.* 2010 , **31**, 224 –247.
23. S. Stoll, J. Schweiger, *J. Magn. Reson.* 2006, **178**, 42-55.
24. (a) E. Bertolomé, P. J. Alanso, A. B. Arauzo, J. Luzón, J. Bertolomé, C. Racles, C. Turta, *Dalton Trans.* 2012, **41**, 10382-10389. (b) S. Gómez-Coca, A. Urtizbera, E. Cremades, P. J. Alonso, A. Camón, E. Ruiz, F. Luis, *Nature Commun.* 2014, **5**, 4300: doi:10.1038/ncomms4300.

25. J. H. van der Waals, Optical Properties of Excited States in Solids, The Study of Paramagnetic Excited States by Electron Paramagnetic Resonance; Springer US: NATO ASI series, 1992, 301.